Strain modulation using defects in two dimensional MoS_2

Kory Burns[1], Anne Marie Z. Tan[1,2], Horace Gordon V[3], Tianyao Wang[4], Adam Gabriel[4], Lin Shao[4], Richard G. Hennig[1,2], and Assel Aitkaliyeva[1*]

[1]*Department of Materials Science and Engineering, University of Florida, Gainesville, FL, 32611, U.S.A.*

[2]*Quantum Theory Project, University of Florida, Gainesville, FL, 32611, U.S.A.*

[3]*Department of Chemical Engineering, University of Florida, Gainesville, FL, 32611, U.S.A.*

[4]*Department of Nuclear Engineering, Texas A&M University, College Station, TX, 77840, U.S.A.*

We investigate the nature of strain in MoS_2 and correlate it to defect types and densities, while systematically assessing the tolerance of this low dimensional material to He and Au ion irradiations. Through a series of theoretical predictions and experimental observations, we establish the onset of the crystalline-to-amorphous transition in MoS_2 and identify sulfur vacancies as the most favorable defects introduced during irradiation. We note the presence of both tensile and compressive strains, which depend on the types of defects introduced into the lattice and vary with increasing fluence. The results show that defects can be used to tune strain in two-dimensional materials and provide an exciting pathway for using external stimuli to control properties of low dimensional materials.

*Corresponding author: aitkaliyeva@mse.ufl.edu (Assel Aitkaliyeva)

INTRODUCTION

It has been long postulated that strain can be used to control the electronic and topological properties of materials. While significant progress has been made, controlling and predicting materials properties at the level of electrons and atoms requires a fundamental understanding of the correlation between strain and structure of materials, which is yet to be achieved. To date, strain has been used to enhance electron mobility in bulk Si [1], improve photocatalytic properties of semiconductor-oxide thin films [2], and tune optical [3-6], thermal [7], and magnetic [8-10] properties of two-dimensional (2D) materials. Throughout their lifetime, 2D materials can be exposed to high temperatures and particle irradiation environments, which pushes the material away from equilibrium.

For example, 2D molybdenum disulfide (MoS_2) has been pushed away from equilibrium using various methods, including fabrication processes [11], electron beam irradiation [12-14], ion beam irradiation [15-17], electromagnetic radiation [18], hydrostatic pressure [19], and chemical doping [20]. While we understand that these processes introduce defects, which act as the primary source of strain [21], the relationship between defects and strain, and their influence on properties of 2D materials are not well understood. The most common extrinsic point defects found in MoS_2 crystals are carbon and oxygen substitutional impurities [22, 23], and the most common intrinsic defect type is the sulfur vacancy [12, 14]. However, visualizing the dissimilarity between vacancies and these substitutional atoms remains a significant challenge because the subtle contrast changes challenge current transition-electron microscopy (TEM) methods [24]. Recent advances in microscopy will allow the direct visualization of the substitutional oxygen on chalcogen vacancy sites in the future [25]. Since substitutional oxygen can occupy vacant lattice

sites and thus alter properties of MoS_2 [17], understanding the types of defects that are introduced into this 2D material is paramount to being able to control its properties and thus using it in devices.

In this work, we employ high-resolution transition-electron microscopy (HR-TEM) to monitor the atomic scale evolution of MoS_2 under ion irradiation. Irradiation is one of the simplest ways to introduce an abundance of defects into the system and push the material further away from equilibrium. As the fluence and vacancy concentration increase, the material's properties evolve from being dominated by isolated point defects to defect clusters. By coupling our findings with first-principles calculations, we identify the most likely point defects and analyze their effect on the biaxial strain. Additionally, we use chemical analysis to confirm that sulfur vacancies are the dominant defects found in our material. Finally, we discuss jointly how intrinsic and extrinsic point defects impact biaxial strain in MoS_2.

I. METHODOLOGY

A. Experimental details

Freestanding MoS_2 sheets were prepared by a sono-chemical synthesis of monolayer MoS_2 powder submerged in N, N-dimethylformamide at a concentration of 15 mg/mL, sonicated for 1 hour in order to further reduce the dimensionality of the flakes, and dispersed on holey carbon TEM grids. The prepared specimens were plasma cleaned for 25 seconds prior to characterization, then analyzed in an FEI Tecnai F20 scanning/TEM (S/TEM) operated at 80 keV. A representative example of a HR-TEM micrograph of as-fabricated 2H-phase MoS_2 is provided in Fig. 1(a), with a magnified view of the atomic arrangements and corresponding location of Mo and S atoms in simulated MoS_2 lattice shown in Fig. 1(b). Note that the instrument used for characterization of these specimens was not aberration corrected, and we relied on energy dispersive spectroscopy

(EDS) scans to verify the composition of the specimens and identify the locations of Mo and S atoms in the lattice.

To calculate the lattice parameter, a_0, we utilized a fast Fourier transformation (FFT) methodology; an example of an FFT image is shown as an inset in Fig. 1(a). This approach allows us to convert the structural micrograph to reciprocal space, masking along the [110] crystallographic direction to generate an inverse FFT (IFFT) image, and filtering out the electron waves that do not produce lattice fringes in the desired [110] crystallographic direction needed to calculate a_0 and d_{110} spacings, as illustrated in Fig. 1(b). The lattice spacing measurements were averaged over 300 measurements for unirradiated and ~600 measurements for each irradiated specimen. The measured $a_0 = 3.184$ Å and $d_{110} = 1.592$ Å values for unirradiated flakes are in good agreement with the values reported in the literature [26-29] and our theoretical predictions. Figure 1(d) shows the typical line intensity profile of an MoS_2 lattice when scanned in the direction of the white arrow shown in Fig. 1(c). The intensities emitted in the profile are atom-specific, where Mo atoms emitted an intensity at ~ 550 and S atoms emitted at ~ 430. The intensity variation is easier to discern in pristine monolayer sheets of MoS_2 than bulk sheets due to the stacking arrangement of Mo on top of S atoms in layered materials.

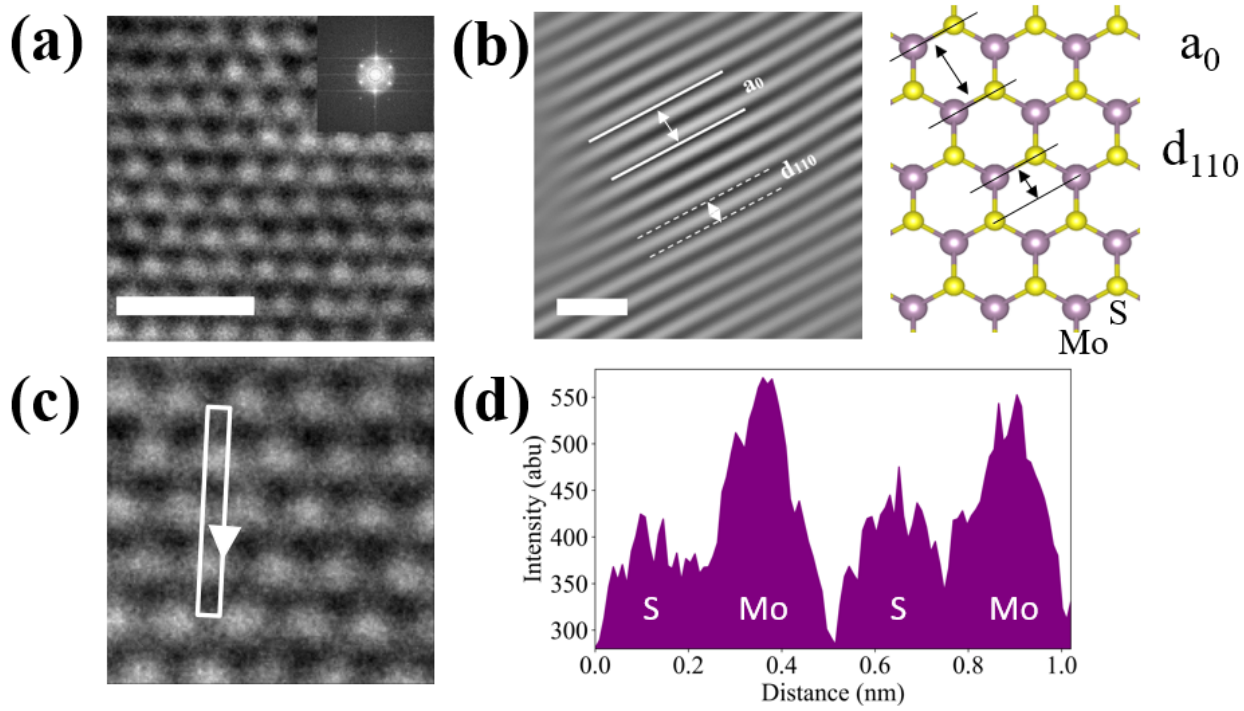

FIG. 1. (a) HR-TEM micrograph of as-fabricated MoS_2, where the scale bar denotes 1 nm. (b) Inverse FFT image used to calculate lattice spacing in the material, with a_0=3.18Å and d_{110}=1.59Å. Here the scale bar denotes 5Å. Additionally, a schematic of the MoS_2 structure is provided on the right, in which yellow atoms are S, and purple atoms are Mo. (c) Magnified view of the area shown in (a). The inset in the micrograph depicts the line profile of the EDS scan shown in (d), with the arrow identifying the scan direction. (d) Line scan of the area shown in (c) that identifies the positions of S and Mo atoms in the lattice.

Following pre-irradiation characterization, specimens were subjected to 120 keV He^+ and 3 MeV Au^{2+} ion irradiations at room temperature using 150 keV single-ended accelerator and 1.7 MeV General Ionex tandem accelerator, respectively. The ion fluence ranged from 1×10^{12} to 1×10^{17} cm^{-2} for the He ion irradiation and 1×10^{12} to 1×10^{16} cm^{-2} for the Au ion irradiation. The area of the beam was 6×9 mm^2 and 11×12 mm^2 for the He and Au irradiations, respectively, while

the angle of incidence was approximately 0°. The target chamber pressure during irradiation was ~6×10^{-8} torr. Upon completion of irradiation experiments, specimens were re-characterized in the same fashion as described earlier.

B. Computational details

We computed defect formation energies and defect-induced changes in the lattice constant using density functional theory (DFT) as implemented in the Vienna ab initio simulation package (VASP) [30]. We performed calculations using the projector-augmented wave method [31, 32] and treated the exchange-correlation using the Perdew-Burke-Ernzerhof (PBE) [33] generalized gradient approximation functional. We employed a plane-wave cutoff energy of 520 eV for the plane-wave basis set and Methfessel-Paxton smearing [34] with a smearing energy width of 0.10 eV, and Γ-centered Monkhorst-Pack *k*-point meshes as described below [35] for the Brillion zone integration.

We have considered the effects of eight types of vacancies and vacancy clusters (see Fig. S1 for schematic illustrations of each type of vacancy or vacancy cluster), four configurations of S interstitials or adatoms (Fig. S2), and two types of O atom or molecule adsorptions on the S vacancy site (Fig. S3). A few additional configurations for the interstitials and adatoms were considered but were found to be unstable; here, we have reported only the sites that we found to be at least metastable after structural relaxation. In this study, we have considered only the neutral charge states for all defects. The effect of charged defects may be considered in a future study.

To estimate the likelihood for each type of defect to be formed under irradiation, we first computed the formation energy of each defect under equilibrium conditions. The formation energy

$E^{\text{form}}[X]$ of a neutral point defect X is determined by DFT calculations using a supercell approach following:

$$E^{\text{form}}[X] = E_{\text{tot}}[X] - E_{\text{tot}}[\text{pristine}] - \Sigma_i\, n_i\mu_i \quad (1)$$

where $E_{\text{tot}}[X]$ and $E_{\text{tot}}[\text{pristine}]$ are the total DFT-derived energies of the supercell containing the defect X and the pristine supercell, respectively, n_i is the number of atoms of species i added or removed, and μ_i is the corresponding chemical potential of the species. The relevant chemical potentials were chosen to be $\mu_{\text{Mo}} = \mu_{\text{bccMo}}$, $\mu_{\text{S}} = (\mu_{\text{MoS}_2} - \mu_{\text{bccMo}})/2$, and $\mu_{\text{O}} = \mu_{\text{O}_2(\text{gas})}/2$, corresponding to Mo-rich conditions. Defect calculations were performed in 2×2×1, 3×3×1, 4×4×1, and 5×5×1 supercells, with 20 Å vacuum spacing between layers, and k-point meshes corresponding to about a 12×12×1 k-point mesh per hexagonal unit cell of monolayer MoS_2 (≈ 400 k-points per reciprocal atom in 2D). To evaluate the defect formation energies, we applied periodic boundary conditions, fixed the supercell lattice vectors, and relaxed all atomic positions. We report the defect formation energies in the dilute limit, by assuming a $1/L^2$ supercell size dependence due primarily to elastic interactions between periodic images and extrapolating to the $L \to \infty$ limit.

Where appropriate, we also evaluated the binding energy E^{bind} for the formation of vacancy clusters, or for the binding of O atoms or molecules to a S vacancy site. For the vacancy clusters, E^{bind} is defined relative to the isolated molybdenum and sulfur vacancies as follows:

$$E^{\text{bind}}[\text{V}_{\text{Mo}_x\text{S}_y}] = E^{\text{form}}[\text{V}_{\text{Mo}_x\text{S}_y}] - x\, E^{\text{form}}[\text{V}_{\text{Mo}}] - y\, E^{\text{form}}[\text{V}_{\text{S}}]. \quad (2)$$

For the adsorbed O and O_2, the binding energy is defined as the difference between the respective O_S or $(O_2)_S$ formation energy and the V_S formation energy:

$$E^{\text{bind}}[\text{O}_{\text{S}}] = E^{\text{form}}[\text{O}_{\text{S}}] - E^{\text{form}}[\text{V}_{\text{S}}] \quad (3)$$

$$E^{\text{bind}}[(\text{O}_2)_{\text{S}}] = E^{\text{form}}[(\text{O}_2)_{\text{S}}] - E^{\text{form}}[\text{V}_{\text{S}}]. \quad (4)$$

We estimated the changes in lattice constant induced by different concentrations of each defect by again constructing 2×2×1, 3×3×1, 4×4×1, and 5×5×1 supercells, each containing a single defect or defect cluster, but this time allowing the supercell lattice vectors to relax as well. For comparison to experimental results, and assuming a random orientation of defects in a specimen, we report the average change of the in-plane lattice constants.

II. RESULTS

A. Inducing strain in MoS_2 using irradiation

We display the effect of irradiation on the structure of MoS_2 in Figs. 2 and 3. Note that the HR-TEM micrograph of the starting microstructure provided in Fig. 1(a) captures intrinsic defects in as-fabricated flakes, which were accounted for prior to irradiation experiments. It is known that prolonged imaging of specimens in the TEM can induce defects [12, 14], and thus precautions were taken to distinguish between electron beam damage and ion irradiation-induced defects. All specimens were imaged in the TEM at 80 keV, exposed to an electron beam for approximately the same duration and dwell time, and imaged at consistent magnification settings to maintain both fluence (~3.96×10^{7} nm^{-2}) and flux (~4.4×10^{5} $nm^{-2}\cdot s^{-1}$) of electrons equivalent for all examined specimens, including unirradiated and irradiated MoS_2.

Figure 2 shows the evolution of the MoS_2 atomic structure with increasing He ion fluence. As expected, the lattice becomes more distorted with increasing fluence. However, as can be evidenced from the provided HR-TEM micrographs, the material does not undergo a crystalline-to-amorphous transition. As shown in Figure 2, specimens irradiated to the highest He ion fluence of 1×10^{17} cm^{-2} remain crystalline in nature. Figure 3 depicts the MoS_2 lattice becoming progressively more distorted as the Au ion fluence is systematically increased from 1×10^{12} to

5×10^{14} cm^{-2}. The specimens remained crystalline through a fluence of 1×10^{14} cm^{-2} when some amorphous regions were starting to develop. However, at 5×10^{14} cm^{-2}, the specimen went through a complete crystalline-to-amorphous transition, as can be evidenced from the HR-TEM micrographs.

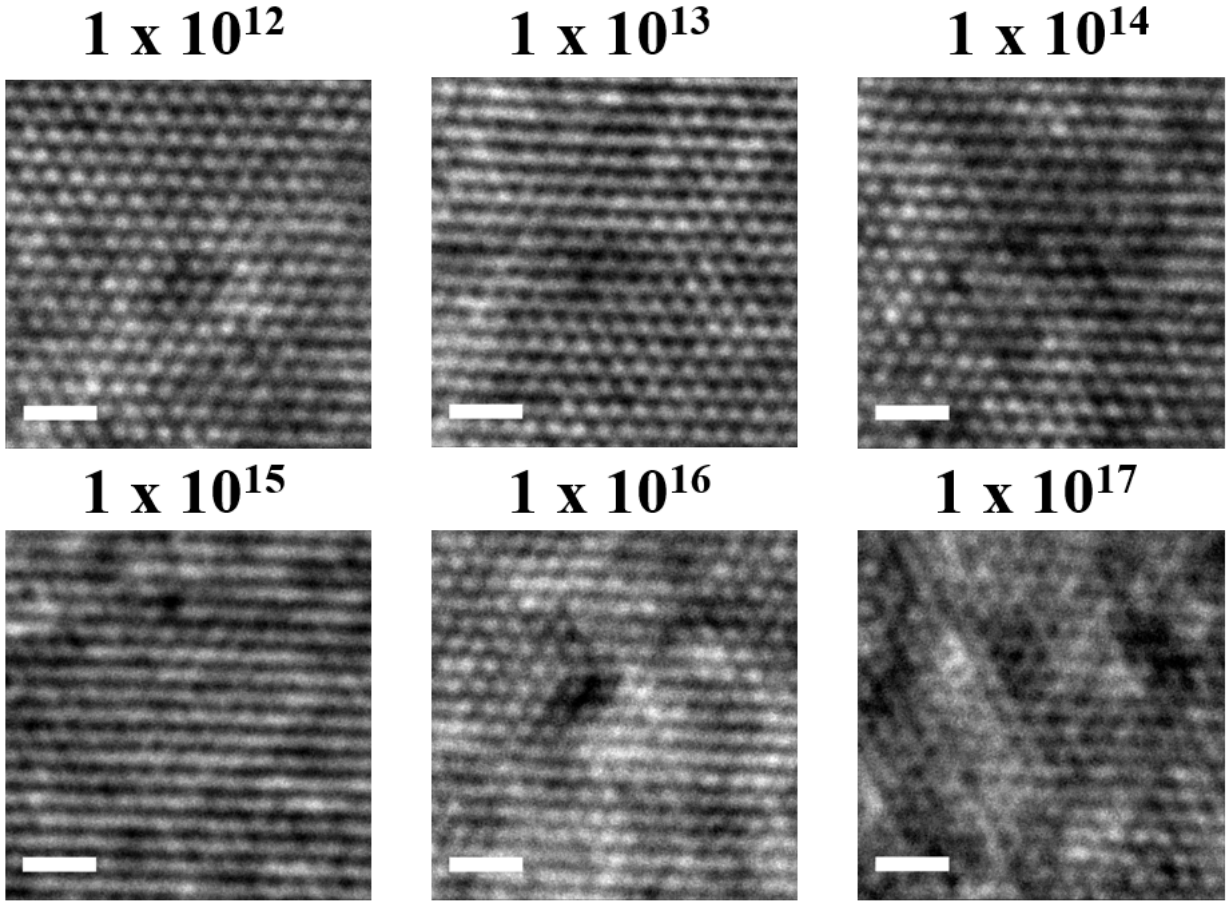

FIG. 2. Bright-field TEM micrographs of MoS_2 specimens irradiated with 120 keV He^+ ions to fluences ranging from 1×10^{12} cm^{-2} to 1×10^{17} cm^{-2}. The scale bars denote 1nm in all provided micrographs.

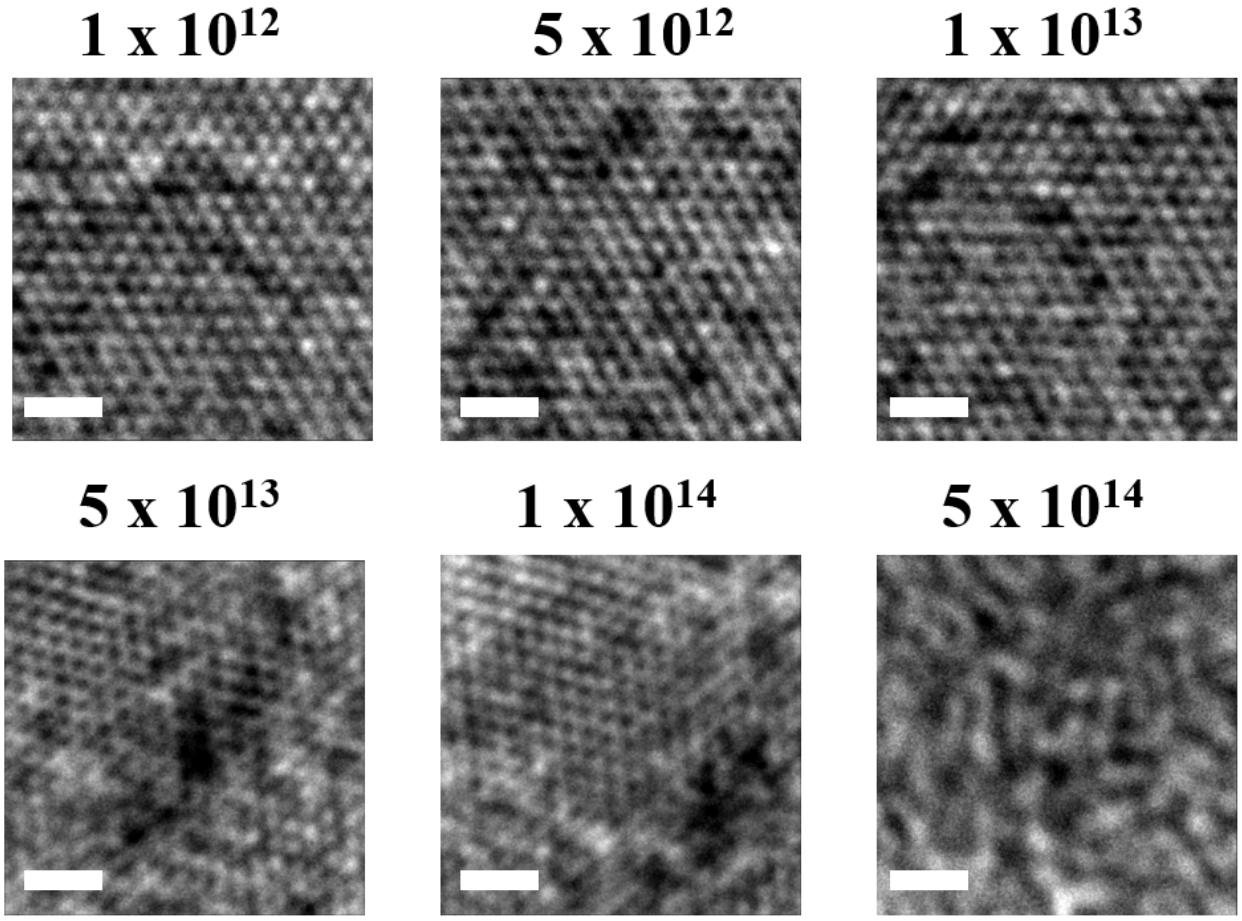

FIG. 3. Bright-field TEM micrographs of MoS_2 specimens irradiated with 3 MeV Au^{2+} ions to fluences ranging from 1×10^{12} cm^{-2} to 5×10^{14} cm^{-2}. The scale bars denote 1 nm in all provided micrographs.

We further analyzed the micrographs and measured the change in lattice parameter, a_0, in MoS_2 with ion fluence and correlated it to the strain $\Delta a_0/a_0$ induced by defects in the material. Figure 4(a) plots the change in lattice constant for both ion species, while Figure 4(b) plots the S:Mo atomic ratio as a function of ion fluences. From both of our irradiation experiments, we observe noticeable changes in lattice strain, which will be discussed in depth in the discussion section together with the computational results. Complementary to imaging, we utilized EDS

measurements to determine the EDS intensity ratios for Mo and S to identify which defect type dominates the irradiation response of our material. As can be seen from Fig. 4(b), the sputtering rate of S atoms is vastly more efficient than the rate at which Mo atoms are displaced from the lattice for both ion species, which indicates that S:Mo ratios approach saturation at higher fluences. This can be attributed to reduced S sites for displacements at higher fluences, under preferential S sputtering.

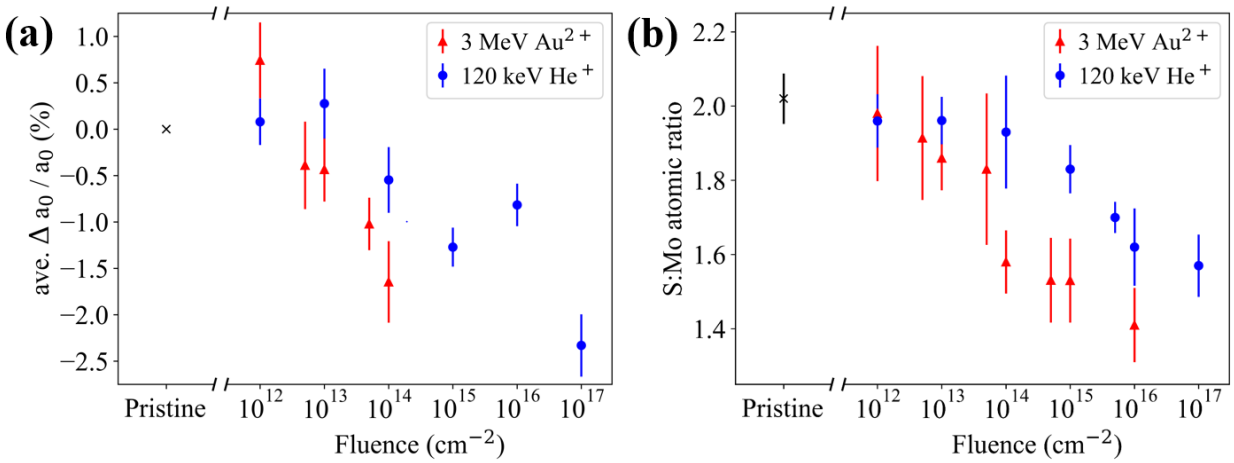

FIG. 4. (a) The relationship between strain $\Delta a_0/a_0$ and fluence of the ion species, and (b) plot of the relationship between S:Mo atomic ratio and increasing ion fluence.

B. Computational modeling of defects and strain

Complementary to the experimental work, we utilized DFT calculations to understand the defect types governing the radiation-induced strain response of this low dimensional material. We started by considering which defects are most energetically favorable in MoS_2. Table 1 lists the formation and binding energies for all considered defects. Out of all the vacancies and vacancy clusters, the single and double S vacancies are by far the most energetically favorable. This is in

agreement with previous studies, which also predicted that S vacancies are the most likely intrinsic defect in MoS_2 [36-38]. The formation energy for Mo vacancies is much higher, which suggests that most of the vacancies generated are likely to be S vacancies. Our calculations also suggest that Mo vacancies are more likely to be created next to existing S vacancies, e.g., in the case of V_{MoS} and V_{MoS_3}.

TABLE I. Formation energies E^{form} and binding energies E^{bind} for all the defects considered in this study. For each defect, E^{form} is calculated following Eq (1) and, where relevant, E^{bind} is calculated following Eq (2), (3), or (4) as appropriate. The values in parentheses indicate the difference between the formation energy evaluated based on a 5×5 supercell and that estimated based on extrapolation to the dilute limit.

	E^{form} (eV)	E^{bind} (eV)
Vacancies:		
V_S	1.23 (0.02)	
$V_{S_2(c)}$	2.40 (0.08)	–0.06
$V_{S_2(p)}$	2.38 (0.09)	–0.08
V_{Mo}	7.19 (0.02)	
V_{MoS}	6.49 (0.01)	–1.93
V_{MoS_2}	7.35 (0.04)	–2.30
V_{MoS_3}	5.49 (0.02)	–5.39
V_{MoS_6}	9.17 (0.25)	–5.40
S interstitials:		

$S_{ad\text{-}S}$	2.46 (0.01)	
$S_{int\text{-}split}$	7.90 (0.09)	
$S_{int\text{-}hex1}$	7.36 (0.34)	
$S_{int\text{-}hex2}$	8.71 (0.23)	
O impurities:		
O_S	–2.71 (0.03)	–3.94
$(O_2)_S$	–0.56 (0.02)	–1.79

In addition, formation energies for four S adatom and interstitial defects have been calculated. The S adatom directly on top of another S atom in the monolayer is by far the most energetically favorable configuration; however, we expect adatoms to have minimal effect on the lattice constant. Hence, we have also considered several S interstitial configurations. The three configurations listed were found to be metastable, but with high formation energies of greater than 7 eV. However, under the highly non-equilibrium conditions present during irradiation, such defects may be created, for example, as part of a damage cascade.

Figure 5 shows the average change in the in-plane lattice parameters induced by a variety of defects in monolayer MoS_2, computed with DFT. The defects plotted in Fig. 5 include the five lowest energy vacancies and vacancy clusters (V_S, $V_{S_{2(c)}}$, $V_{S_{2(p)}}$, V_{MoS}, V_{MoS_3}), and adsorption of an O atom or molecule at a S vacancy site. The results for the remaining defects are presented for completeness in Fig. S3.

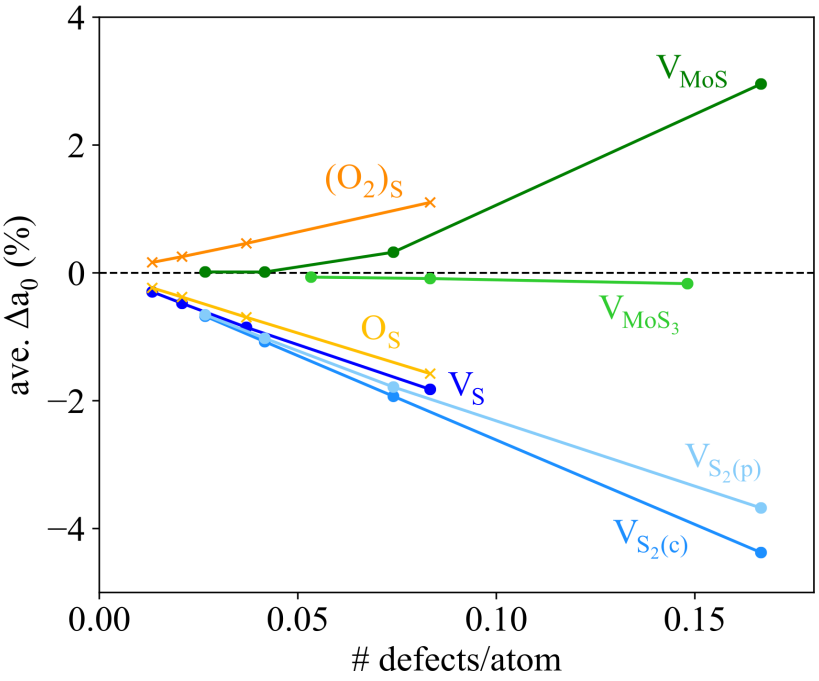

FIG. 5. Average induced strain, $\Delta a_0/a_0$ in percent for monolayer MoS_2 as a function of defect (vacancy/adatom/interstitial/substitutional) concentration. All the shown vacancies and vacancy clusters cause lattice contraction, except for V_{MoS}. Meanwhile, the O_2 molecule adsorbed on a S vacancy site causes lattice expansion.

III. DISCUSSION

A. Which defect type dominates the response of MoS_2 to irradiation?

The range of defect concentrations modeled with DFT is limited compared to what one would expect to find in samples irradiated under different fluences spanning orders of magnitude. Hence, we do not attempt to make a direct comparison of the experimental data with computational results. Instead, we use our DFT predictions as a guide to which defect types dominate the radiation-induced strain response of free-standing MoS_2 and ascertain the validity of our assumptions.

Electronic collisions, in which impinging particles excite or eject electrons from the material, dominate at high energies, while nuclear collisions dictate the response of the material at low energies. Based on the selected irradiation conditions, the primary damage mechanism in these free-standing MoS_2 specimens is the ballistic collisions between impinging ions and target atoms. Every energetic particle encountering the lattice displaces either a Mo or S atom from their lattice sites, which are now considered primary knock-on atoms (PKA) and indicate the initiation of a displacement cascade. In a bulk material, once PKA loses energy during displacement series, it can become an interstitial in a lattice site. However, we believe that in low dimensional materials such as MoS_2 examined in this study, displaced atoms will primarily be ejected from the lattice, thus leaving predominantly vacancies along the ion tracks.

We recognize that while the energy to displace an atom under irradiation is not equivalent to the formation energy of defects calculated under dilute, equilibrium conditions, they are likely to be correlated [12]. Nonetheless, a comparison of the relative formation energies can still provide insight into the types of defects that are more likely to be created in MoS_2 under irradiation. For example, Komsa *et al.* [12] calculated displacement threshold energies for atoms in transition metal dichalcogenides including MoS_2, and estimated that the minimum initial kinetic energy required to sputter a S atom from monolayer MoS_2 would range from about 6.9 eV (S from bottom layer) to 8.1 eV (S from top layer), while it would take about 20 eV to displace a Mo atom.

Based on the displacement energy alone, the displacement of S atoms is more energetically favorable. However, the displacement energy represents the cutoff energy value needed to completely displace an atom from its lattice site and does not account for atomic mass number of the projectile or target atoms, which makes it not ideal for determining the damage production efficiency in an irradiated material. To mitigate this, we correlated the displacement energy values

to vacancy production efficiency in MoS_2 using Boltzmann transport equation method described in [39]. In case of He ion irradiation, the calculated displacement cross-section values were 0.164 $Å^2$ for Mo and 0.707 $Å^2$ for S (values were calculated for the bottom layer). For Au ion irradiation, cross-sections for the defect production were 0.046 $Å^2$ (Mo) and 0.088 $Å^2$ (S from bottom layer). These values are in the same order of magnitude as the cross-sections reported for other low dimensional materials in the past [40]. As evidenced by higher displacement cross-section values, the formation of S vacancies is the most energetically favorable, and thus, one should expect a more rapid depletion of S atoms from the lattice.

Our experimental observations indicate that vacancies are indeed the most predominant type of defect observed in all irradiated specimens, regardless of the type of ion species selected for irradiation, which is consistent with the calculated displacement cross-section values. The concentration of vacancies increases with fluence, and since vacancies tend to cluster to reduce overall energy of the system due to the instability of isolated vacancies [41], vacancy agglomeration generally dominates the radiation response of MoS_2 [42]. In our ex-situ experiments, we are unable to account for the kinetics of the defect formation mechanism and hence do not base our justification for large defect sites on the diffusion of vacancies. The negative binding energies provided in Table 1 indicate that it is more energetically favorable for vacancies to be created next to another existing vacancy site, and at high fluences, we observe larger vacancy clusters (Fig. S4). The defect clusters observed are triangular and compact in topology, as opposed to a linear defect formation observed in high-temperature electron irradiation experiments [42] because at room temperature the diffusion rate is relatively slow compared to the rate at which S vacancies are created [43].

We were unable to distinguish between types of vacancies (Mo vs. S) created in irradiated specimens using our instrument, and thus, relied on EDS and XPS measurements to resolve compositional differences in irradiated specimens. Based on EDS data that show decreasing S:Mo ratio with increasing ion fluence, we expect S vacancies to dominate in our specimens, in agreement with theoretical predictions. However, it does not imply that there are no other defect types formed in the material upon irradiation, merely that vacancies (most likely S vacancies) dominate the radiation response of MoS_2.

As can be seen from Figs. 2 and 3, MoS_2 specimens irradiated with heavier Au ions had more damage than those irradiated with lighter He ions. It is hardly surprising to see that damage cascades produced by the larger Au ions are more likely to overlap than those resulting from the smaller He ions. The critical ion fluences required to induce crystalline-to-amorphous transition in MoS_2 is thus much lower for Au-irradiated specimens (5×10^{14} cm^{-2} vs. $>1\times10^{17}$ cm^{-2} for He). While we have not explored what fluence is required to induce the crystalline-to-amorphous transition in He-irradiated MoS_2, the accumulation of damage will lead to eventual amorphization of the specimen. Again, the goal of this study was to examine the amount of strain that intrinsic defects induce in MoS_2, and the provided data indicates that regardless of used ion species, strain is strongly correlated to the extent of damage in the material.

B. Which defects are responsible for the observed biaxial strain?

We have already determined that the radiation response of MoS_2 is vacancy dominated, and to elucidate which defect type is responsible for strain changes in irradiated materials, we use our theoretical predictions. We estimate that the defect concentrations modeled with DFT and plotted in Fig. 5 correspond to the defect concentrations in specimens irradiated to a fluence of

~10^{14} cm^{-2}. If every incoming ion creates one vacancy, a fluence of 10^{14} cm^{-2} will create a vacancy concentration of 10^{14} cm^{-2} ≈ 0.03 vacancies/atom. Alternatively, by assuming that the vast majority of vacancies that are created are S vacancies, S:Mo stoichiometric ratios of 1.91 (10^{14} cm^{-2} He^{+} irradiation) and 1.58 (10^{14} cm^{-2} Au^{2+} irradiation) correspond to vacancy concentrations of ≈ 0.023 and 0.14 vacancies/atom, respectively. These rough approximations provide us with order-of-magnitude estimates for comparing our computational and experimental results; a more detailed prediction of the defect concentrations at different irradiation fluences is beyond the scope of this work. Hence, in the following analysis, we focus on the general trends (lattice expansion or contraction) and order of magnitude estimates, rather than comparing exact values.

Figure 5 shows that single sulfur vacancies generate a compressive strain, while single Mo vacancies generate a tensile strain. Our calculations suggest that most types of vacancies and vacancy clusters lead to a contraction of the lattice in-plane, except for V_{Mo} and V_{MoS}. Due to their low formation energies, we expect that most of the vacancies created during irradiation are S vacancies or contain S vacancies, i.e., it is unlikely that many single Mo vacancies V_{Mo} form. Li *et al.* [44] reported that the two most common defects created under extended electron irradiation of their MoS_2 specimens were V_S and V_{MoS_3}. Since the vacancies and vacancy clusters tend to lead to lattice contraction, this could explain the general trend of increasing lattice contraction with increasing irradiation fluence, as greater numbers of such defects are created in the specimen. The preferential creation of S vacancies by knocking out S atoms also corroborates with the trend of decreasing S:Mo ratio in specimens irradiated to high fluences.

XPS data (Fig. S5) showed a shift in binding energy in correlation to the Mo subshell for the irradiated specimen, which is indicative of Mo-O binding in irradiated specimens. Because of this, we considered two possibilities for the adsorption of O atoms or molecules at existing S

vacancy sites. Oxygen from the atmosphere is one of the most common contaminants, which likely encounters the specimens during sample preparation and/or transfer. We find that it is energetically favorable for either O atoms or molecules to bind to existing S vacancy sites, with O binding more strongly; this is not surprising since O is isoelectronic to S. Hence, it is likely that a significant proportion of the S vacancies that may have been introduced during irradiation would be filled by O atoms or molecules.

Thus, after irradiation, when the specimens are removed from the vacuum environment, we expect that extrinsic defects immediately occupy some of the vacant lattice sites. Our assumptions agree with previously published literature that indicates that at low concentrations of vacancies, substitutional oxygen is more energetically favorable than single sulfur vacancies [14]. As shown in Fig. 5, single O atoms adsorbed on a vacant S site lead to lattice contraction similar to that of an empty S vacancy, however an O_2 molecule adsorbed on a vacant S site causes lattice expansion. While the O_S defect has been found to be significantly more energetically favorable than $(O_2)_S$, the former requires the dissociation of the O_2 molecule, which may be a kinetic barrier to the formation of this defect. The energy levels observed in our XPS spectra of irradiated specimens (Fig. S5) are identified to correspond to Mo-O_2 bonding rather than Mo-O bonding. Hence, we believe that a greater number of S vacancy sites have been filled by O_2 molecules, which could also account for the slight lattice expansion observed at low irradiation fluence.

IV. SUMMARY

In this work, we investigated the amount of biaxial strain induced in irradiated MoS_2 specimens by various defects using a combination of experiments and theoretical predictions. We show that the radiation response of MoS_2 is dominated by vacancies and determine the critical

fluence for the crystalline-to-amorphous transition for Au to be above 1×10^{14} cm^{-2} and above 1×10^{17} cm^{-2} for He. Our data demonstrate that initially, the strain is tensile in nature but transitions to compressive with increasing fluence. The difference stems from the type of defects introduced into the lattice during irradiation. Lower irradiation fluences tend to create single S vacancies, which, when filled by O_2 molecules from the atmosphere, lead to a slight expansion of the lattice. At higher fluences, the creation of more vacancies and the formation of larger vacancy clusters dominates, leading to lattice contraction. Our data proves that various defect configurations can be used to control the orientation and magnitude of the strain, which is the first step towards establishing the fundamental relationship between irradiation-induced defects and properties of MoS_2 and the ability to control properties of low dimensional materials.

ACKNOWLEDGMENTS

The work was supported by the U.S. Department of Energy, Office of Science, Basic Energy Sciences, under Award No. DE-SC0019014 "Establishing defect-property relationships for 2D-nanomaterials." RGH and AMZT were supported by the National Science Foundation under Awards Nos. 1748464 and 1539916. This research used computational resources provided by the University of Florida Research Computing Center (http://researchcomputing.ufl.edu).

References:

1. J. Welser, J. Hoyt, S. Takagi, and J. Gibbons. IEDM Tech. Dig., 373-376 (1994).
2. Z. Liu, J. Shenoy, C. Menéndez, J. N. Hart, C. C. Sorrell, and C. Cazorla. arXiv 1909.00979
3. R. Frisenda, M. Drüppel, R. Schmidt, S. Michaelis de Vasconcellos, D. Perez de Lara, R. Bratschitsch, M. Rohlfing, and A. Castellanos-Gomes. npj 2D Mater Appl **1**, 10 (2017).
4. L. Yang, X. Cui, J. Zhang, K. Wang, M. Shen, S. Zeng, S. A. Dayeh, L. Feng, and B. Xiang. Sci Rep **4**, 5649 (2015).
5. H. Peelaers and C. G. Van de Walle. Phys. Rev. B **86**, 241401(R) (2012).
6. M. Xu, G. Zhan, S. Liu, D. Zhang, X. Zhong, Z. Qu, Y. Li, A. Du, H. Zhang, and Y. Wang. Phys. Rev. B **100**, 235435 (2019).
7. X. Meng, T. Pandey, J. Jeong, S. Fu, J. Yang, K. Chen, A. Singh, F. He, X. Xu, J. Zhou, W. Hseih, A. K. Singh, J. Lin, and Y. Wang. Phys. Rev. Lett. **122**, 155901 (2019).
8. H. Rostami, R. Roldán, E. Cappelluti, R. Asgari, and F. Guinea. Phys. Rev. B **92**, 195402 (2015).
9. J. Son, K. Kim, Y. H. Ahn, H. Lee, and J. Lee. Phys. Rev. Lett. **123**, 036806 (2019).
10. S. Fang, S. Carr, M. A. Cazalilla, and E. Kaxiras. Phys. Rev. B **98**, 075106 (2018).
11. A. Castellanos-Gomez, R. Roldán, E. Cappelluti, M. Buscema, F. Guinea, H. S. J. van der Zant, and G. A. Steele. Nano Lett. **13**, 11, 5361-5366 (2013).
12. H. Komsa, J. Kotakoski, S. Kurasch, O. Lehtinen, U. Kaiser, and A. V. Krasheninnikov. PRL **109**, 035503 (2012).
13. W. M. Parkin, A. Balan, L. Liang, P. Masih Das, M. Lamparski, C. H. Naylor, J. A. Rodríguez-Mano, A. T. Charlie Johnson, V. Meunier, and M. Drndić. ACS Nano **10**, 4134-4142 (2016).

14. H. Komsa, S. Kurasch, O. Lehtinen, U. Kaiser, and A. V. Krasheninnikov. Phys. Rev. B **88**, 035301 (2013).

15. P. Mishra, M. Tangi, T. Ng, M. Hedhili, D. H. Anjum, M. Alias, C. Tseng, L. Li, and B. Ooi. Appl. Phys. Lett. **110** 012101 (2017).

16. S. Mignuzzi, A. J. Pollard, N. Bonini, B. Brennan, I. S. Gilmore, M. A. Pimenta, D. Richards, and D. Roy. Phys. Rev. B **91**, 195411 (2015).

17. Z. He, R. Zhao, X. Chen, H. Chen, Y. Zhu, H. Su, S. Huang, J. Xue, J. Dai, S. Cheng, M. Liu, X. Wang, and Y. Chen. ACS Applied Materials & Interfaces **10** (49), 42524-42533 (2018).

18. J. Lee, M. J. Krupcale, and P. X.-L. Feng. Appl. Phys. Lett. **108**, 023106 (2016).

19. L. Fu, Y. Wan, N. Tang, Y. Ding, J. Gao, J. Yu, H. Guan, K. Zhang, W. Wang, C. Zhang, J. Shi, X. Wu, S. Shi, W. Ge, L. Dai, and B. Shen. Sci Adv 3 **11**, e1700162 (2017).

20. K. Zhang, S. Feng, J. Wang, A. Azcatl, N. Lu, R. Addou, N. Wang, C. Zhou, J. Lerach, V. Bojan, M. J. Kim, L. Chen, R. M. Wallace, M. Terrones, J. Zhu, and J. A. Robinson. Nano Lett. **15**, 6586-6591 (2015).

21. M. Sensoy, D. Vinichenko, W. Chen, C. M. Friend, and E. Kaxiras. Phys. Rev. B **95**, 014106 (2017).

22. R. Addou, L. Colombo, and R. M. Wallace. ACS Appl. Mater. Interfaces **7**, 11921−11929 (2015).

23. R. Addou, S. McDonnell, D. Barrera, Z. Guo, A. Azcatl, J. Wang, H. Zhu, C. L. Hinkle, M. Quevedo-Lopez, H. N. Alshareef, L. Colombo, J. W. P. Hsu, and R. M. Wallace. ACS Nano **9**, 9, 9124-9133 (2015).

24. O. L. Krivanek, M. F. Chisholm, V. Nicolosi, T. J. Pennycook, G. J. Corbin, N. Dellby, M. F. Murfitt, C. S. Own, Z. S. Szilagyi, M. P. Oxley, S. T. Pantelides, and S. J. Pennycook. Nature **464**, 571-574 (2010).

25. S. Barja, S. Refaely-Abramson, B. Schuler, D. Y. Qiu, A. Pulkin, S. Wickenburg, H. Ryu, M. M. Ugeda, C. Kastl, C. Chen, C. Hwang, A. Schwartzberg, S. Aloni, S.-K. Mo, D. Frank Ogletree, M. F. Crommie, O. V. Yazyev, S. G. Louie, J. B. Neaton, and A. Weber-Bargioni. Nat. Commun. **10**:3382 (2019).

26. A. Molina-Sánchez and L. Wirtz. Phys. Rev. B **84**, 155413 (2011).

27. L. Zhang, P. Bompoulis, A. N. Rudenko, Q. Yao, A. van Houselt, B. Poelsema, M. I. Katsnelson, and H. J. W. Zandvliet. Phys. Rev. Lett. **116**, 256608 (2016).

28. K. A. N. Duerloo, Y. Li, and E. J. Reed. Nat. Commun. **5**:4214 (2014).

29. K.-K. Liu, W. Zhang, Y. H. Lee, Y. C. Lin, M. T. Chang, C. Y. Su, C. S. Chang, H. Lai, Y. Shi, H. Zhang, C. S. Lai, and L. J. Li. Nano Lett. **12**, 1538-1544 (2012).

30. G. Kresse and J. Furthmülle. Phys. Rev. B **54**, 11169 (1996).

31. P. E. Blöchl. Phys. Rev. B **50**, 17953 (1994).

32. G. Kresse and D. Joubert. Phys. Rev. B **59**, 1758 (1999).

33. J. P. Perdew, K. Burke, and M. Ernzerhof. Phys. Rev. Lett. **77**, 3865 (1996).

34. M. Methfessel and A. T. Paxton. Phys. Rev. B **40**, 3616 (1989).

35. H. J. Monkhorst and J. D. Pack. Phys. Rev. B **13**, 5188 (1976).

36. J.-Y. Noh, H. Kim, and Y.-S. Kim. Phys. Rev. B **89**, 205417 (2014).

37. H.-P. Komsa and A. V. Krasheninnikov. Phys. Rev. B **91**, 125304 (2015).

38. S. Haldar, H. Vovusha, M. Yadav, O. Eriksson, and B. Sanyal. Phys. Rev. B **92**, 235408 (2015).

39. L. Shao. Nuclear Instruments and Methods in Physics Research B **268**, 3564–3567 (2010).

40. A. V. Krasheninnikov, and K. Norlund. J. Appl. Phys. **107**, 071301 (2010).

41. R. E. Smallman and R. J. Bishop. Modern Physical Metallurgy and Materials Engineering. 6th ed. (1999).

42. Q. Chen, H. Li, S. Zhou, W. Xu, J. Chen, H. Sawada, C. S. Allen, A. I. Kirkland, J. C. Grossman, and J. H. Warner. *ACS Nano* **12**, 7721-7730 (2018).

43. S. Wang, H. Li, H. Sawada, C. S. Allen, A. I. Kirkland, J. C. Grossman, and J. H. Warner, Nanoscale **9**, 6417−6426 (2017).

44. M. Li, Y. Wan, L. Yu, Y. Yang, and J. Lou. Nanoscale Research Letters **11**:155 (2016).